PCCP

PAPER

Cite this: *Phys. Chem. Chem. Phys.*, 2015, **17**, 31887

Molecular dynamics simulations of the enhanced recovery of confined methane with carbon dioxide

Quanzi Yuan, Xueyan Zhu, Kui Lin and Ya-Pu Zhao*

Received 2nd November 2015,
Accepted 5th November 2015

DOI: 10.1039/c5cp06649b

www.rsc.org/pccp

For the first time, the enhanced recovery of confined methane (CH_4) with carbon dioxide (CO_2) is investigated through molecular dynamics simulations. The adsorption energy and configuration of CH_4 and CO_2 on the carbon surface were compared, which shows that CO_2 is a good candidate in displacing confined CH_4. The energy barrier required for displacing CH_4 by CO_2 injection was found to depend on the displacement angle. When CO_2 approached vertically to the carbon surface, the displacement of CH_4 occurred most easily. The curvature and size effects of the carbon nanopores on CH_4 recovery were revealed and indicated that there exists an optimum pore size making the displacement occur most efficiently. The underlying mechanisms of these phenomena were uncovered. Our findings and related analyses may help to understand CO_2 enhanced gas recovery from the atomic level and assist the future design in engineering.

Introduction

Over the last decade, the shale gas, which is primarily composed of methane (CH_4), has grown in importance as a renewable energy source, because of its wide distribution, abundant reserves and low pollution.[1,2] Shale gas is stored in shale reservoirs. The shale has large internal surface area and strong affinity for gases such as methane, hydrogen and *etc.* In addition, a significant part of the pores distributed in the shale is on the nanometer scale.[3–5] Therefore, a large proportion of natural gas in shale reservoirs is in an adsorbed state adsorbing in the nanopores.[6] Owing to the low porosity and low permeability of the shale,[7–10] a variety of technical difficulties in the shale gas extraction urgently require effective methods to enhance the shale gas recovery (ESGR), especially in the organic-rich shale. Recently, the use of supercritical carbon dioxide (CO_2) in ESGR attracts widespread interest because of its low price, general accessibility and its physical–chemical properties.[11] For example, supercritical CO_2 is a better fracturing fluid, because of its lower viscosity and similar density compared with water.[12] Its surface tension is nearly zero, therefore it could easily flow into nanopores. Since CO_2 has a stronger affinity for the shale surface compared with CH_4, CO_2 injection has proved to be a potential way to displace CH_4 in ESGR.[13,14] Compared with other techniques, using CO_2 to displace CH_4 is a feasible, efficient, economic and sustainable method in shale gas exploitation.[15–19]

State Key Laboratory of Nonlinear Mechanics, Institute of Mechanics, Chinese Academy of Sciences, Beijing 100190, China. E-mail: yzhao@imech.ac.cn

The investigations on the adsorption of gas on the shale surface and the displacement of shale gas by injecting CO_2 are important in ESGR. Gubbins and coworkers studied the influence of pore geometry on the design of microporous materials for methane storage.[20–22] And they reported that there exits an optimum pore size that maximizes the excess adsorption. At 274 K, the optimal material for methane storage is a porous carbon having a pore size large enough to contain two adsorbed layers of methane. Busch, Gensterblum and Krooss studied the sorption and desorption behavior of CH_4 and CO_2 on a set of well-characterized coals.[23] Wilcox *et al.* explored the influence of the pore size on CH_4 adsorption in microporous carbon systems.[3] Recently, Zhu and Zhao investigated the atomic mechanisms of CH_4 adsorption in carbon nanopores and established the equation of state for the adsorbed phase.[24] Jessen, Tang and Kovscek explored the unsteady flow of gas mixtures through one-dimensional coal systems to study the enhanced methane recovery by gas injection.[25] Shi and Durucan developed a bidisperse pore-diffusion model for the displacement and desorption of CH_4 in coal by CO_2 injection.[26] However, the atomic mechanisms of the displacement of adsorbed CH_4 by CO_2 injection are far from being well understood.

In this paper, the enhanced recovery of confined CH_4 with CO_2 is investigated using molecular dynamics (MD) simulations to reveal the mechanisms for the displacement of adsorbed CH_4 by CO_2 injection from the atomic level for the first time. Firstly, the comparison between the adsorption of CH_4 and CO_2 on graphene was made in the aspects of energy, configuration, adsorption structure, adsorption capacity and *etc.*,

which are fundamental for investigating the displacement of adsorbed CH_4 by CO_2 injection. Then, the energy variations in the process of the CO_2-injected displacement of CH_4 on graphene under different situations were explored. The energy barriers, which should be overcome in the displacement process, varied with the displacement angle. Based on these results, the process and efficiency of the displacement of CH_4 by CO_2 injection in carbon nanotubes (CNTs) were further investigated. The effect of the CNT diameter on the adsorption and displacement was quantitatively revealed. It was found that there exists an optimum CNT diameter. In CNTs with this optimum diameter, the injecting CO_2 could displace the adsorbed CH_4 with the highest efficiency. The underlying mechanism of this phenomenon was uncovered. Our findings and related analyses may help to understand the CO_2 ESGR from the atomic level and assist the future design in engineering.

Model and method

Molecular dynamics (MD) simulations implemented in the LAMMPS[27] have been carried out to explore the CO_2 enhanced shale gas recovery. The focus is on the underlying mechanisms for the displacement of adsorbed CH_4 by CO_2 injection and how the pore size influences the displacement. In the first place, the displacement of CH_4 molecules by injecting CO_2 molecules on the graphene surface was investigated. The *NVT* ensemble (constant number of atoms, volume and temperature) was used. The Nosé–Hoover thermostat with a time-step of 1 fs was employed to regulate the temperature at 300 K.

The CVFF (consistent valence force field)[28] was adopted to predict the adsorption/desorption behaviors of CH_4 and CO_2 on graphene. The total potential energy consists of two parts: the bond energy B and the nonbond energy E. B is the sum of the bond, angle and torsion energy:

$$B = \sum_{\text{bonds}} k_b(l - l_0)^2 + \sum_{\text{angles}} k_a(\theta - \theta_0)^2 + \sum_{\text{torsions}} k_t[1 + \cos(n\phi - \phi_0)]. \quad (1)$$

The first term represents the energy between covalently bonded atoms, where k_b, l and l_0 are respectively the spring constant of the harmonic bond, real and equilibrium bond distance. The second term represents the energy due to the geometry of electron orbitals involved in covalent bonding, where k_a, θ and θ_0 are, respectively, the force constant of the angle bond, real and equilibrium angle. The third term represents the energy for twisting a bond due to the bond order and neighboring bonds, where k_t, n, ϕ and ϕ_0 are, respectively, the force constant, the periodicity, the dihedral angle and the factor phase. E_{ij} between two atoms i and j separated by r_{ij} is the sum of Lennard-Jones (LJ) and electrostatic potential energy:

$$E_{ij} = 4\varepsilon_{XY}\left[\left(\frac{\sigma_{XY}}{r_{ij}}\right)^{12} - \left(\frac{\sigma_{XY}}{r_{ij}}\right)^{6}\right] + k_e\frac{q_X q_Y}{r_{ij}}, \quad (2)$$

where ε_{XY} is the LJ potential well depth, σ_{XY} is the zero-potential distance. X and Y represent the types of atoms. k_e is the electrostatic constant. The parameters of CVFF used in the MD simulations are listed in Table 1. The values of ε and σ between elements were calculated according to the Lorentz–Berthelot (LB) rule: $\sigma_{XY} = (\sigma_{XX} + \sigma_{YY})/2$ and $\varepsilon_{XY} = (\varepsilon_{XX} \times \varepsilon_{XY})^{1/2}$.

Table 1 Parameters of CVFF used in the MD simulations

Bond parameters		
Bond type	k_b (kcal mol^{-1} nm^{-2})	l_0 (nm)
C–C in graphene	48000.00	0.1340
C–H in CH_4	34061.75	0.1105
C═O in CO_2	31886.80	0.1300
Angle parameters		
Angle type	k_a (kcal mol^{-1} rad^{-2})	θ_0 (°)
C–C–C in graphene	90.0	120.0
H–C–H in CH_4	39.5	106.4
O═C═O in CO_2	200.0	180.0
Torsion parameters		
Torsion type	k_d (kcal mol^{-1})	n	ϕ_0 (°)
C–C–C–C in graphene	3.37	2	180.0
Nonbond parameters			
Nonbond type	ε (kcal mol^{-1})	σ (nm)	q (e)
C–C in graphene	0.148	0.3617	0.000
C–C in CH_4	0.160	0.3474	−0.400
H–H in CH_4	0.038	0.2450	0.100
C–C in CO_2	0.148	0.3617	0.574
O–O in CO_2	0.228	0.2860	−0.287

In the second place, we focus on how the pore size influences the displacement. CNTs were used as the representation of the pores of the shale to exclude other factors that could influence the displacement, such as pore size distribution, the connectivity of the pore, *etc.* For the simplification of large-scale simulations, a coarse-grained model was used: the molecular structures of CH_4 and CO_2 were ignored, CH_4, CO_2, and CNT carbon atoms were treated as LJ particles. The LJ parameters of CH_4 and CO_2 were obtained by considering both the CVFF force field and the grand canonical Monte Carlo (GCMC) predictions to the thermodynamics data,[29] while those for the CNT carbon atoms were taken from the Steele 10-4-3 potential[30] as shown in Table 2. However, to validate the coarse-grained model, we also performed full-atomic simulations and compared with the results.

The adsorption of CH_4 (or CO_2) in our simulations is physical adsorption.[29] The adsorption energy E_{ad} is defined as

$$E_{ad} = E_{a@s} - E_s - E_a, \quad (3)$$

where $E_{a@s}$, E_a and E_s are the energy of the adsorbent on the substrate, the adsorbent and the substrate, respectively. When the adsorbent is far away from graphene, E_{ab} equals zero.

Table 2 LJ parameters of CH_4, CO_2 and carbon atoms in CNTs

Atom/molecule	ε (kcal mol^{-1})	σ (nm)
CH_4	0.294	0.3751
CO_2	0.481	0.3615
C in CNT	0.056	0.3400

Results and discussion

Adsorption of CH_4 and CO_2 on graphene

Firstly, the potential energy surface of the interaction between CH_4 (or CO_2) and the graphene surface was scanned as shown in Fig. 1. The energy surface indicates that the most stable adsorption site of CH_4 on graphene locates at the hollow site of a carbon ring with one C–H bond pointing outwards the graphene surface. When CH_4 approaches graphene as shown in Fig. 1(b), E_{ad} first decreases from 0 to the lowest E_{ad}, and then increases. The equilibrium distance between CH_4 and graphene is 0.34 nm. From Fig. 1(b), E_{ad} of CH_4 on the graphene surface is -5.9320 kcal mol^{-1}. As shown in Fig. 1(c), the most stable adsorption site of CO_2 on graphene locates at the bridge site of the C–C bond in graphene with two C═O bonds pointing towards the hollow sites of the neighboring carbon rings. When CO_2 approaches graphene as shown in Fig. 1(d), E_{ad} first decreases from 0 to the lowest E_{ad}, and then increases. The equilibrium distance between CO_2 and graphene is 0.35 nm. The corresponding E_{ad} of CO_2 is -7.7092 kcal mol^{-1}. From the results, E_{ad} of CO_2 is about 30% lower than that of CH_4, which implies that CO_2 adsorbs on graphene more easily than CH_4 and can be a good candidate in displacing CH_4.

Then, the atomic configuration of one layer CH_4 (or CO_2) molecules adsorbing on graphene was simulated (Fig. 2). As shown in Fig. 2(c) and (f), the radial distribution function (RDF) shows that the nearest neighbor of CH_4 is about 0.382 nm, which is less than that of CO_2 of about 0.386 nm. The RDF indicates that the number density of CH_4 is a little bit larger than that of CO_2. The adsorption densities of one layer CH_4 and CO_2 on graphene are 7.2979×10^{18} and 6.0152×10^{18} m^{-2}, respectively. The corresponding adsorption energy per unit area of CH_4 and CO_2 on graphene is -0.2561 and -0.3359 J m^{-2}, respectively. The adsorption energy per unit area of CO_2 is about 31.16% lower than that of CH_4, which implies that CO_2 could be a good candidate in displacing CH_4.

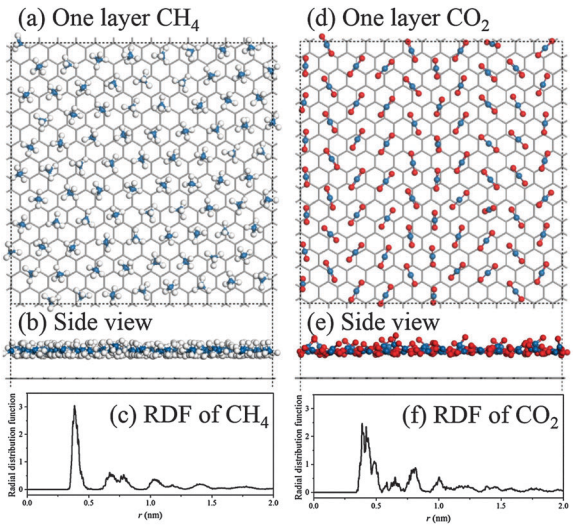

Fig. 2 The atomic configuration of one layer molecules adsorbing on graphene: top view of (a) CH_4 and (d) CO_2; side view of (b) CH_4 and (e) CO_2. The blue, white and red balls represent carbon, hydrogen and oxygen atoms, respectively. The gray lines represent graphene. The radial distribution function (RDF) of (c) CH_4 and (f) CO_2.

Displacement of CH_4 by injecting CO_2 on graphene

We prefer CH_4 molecules to desorb from the substrate rather than adsorbing on the substrate when exploiting shale gas. Therefore, CO_2 molecules were used to displace CH_4 molecules (Fig. 3). The CO_2 molecule was forced to approach the CH_4 molecule with different displacement angle α, which is defined as the angle between the substrate and the route of the CO_2. The rotation of CO_2, CH_4 and the substrate is free in the approaching processes. When $\alpha = 0^\circ$, CO_2 approached CH_4 parallel to graphene; when $\alpha = 90^\circ$, CO_2 approached CH_4 vertically to graphene.

Initially, CH_4 adsorbed at its most stable adsorption site on graphene. This state corresponds to $E = 0$ in Fig. 4(a)–(e). When

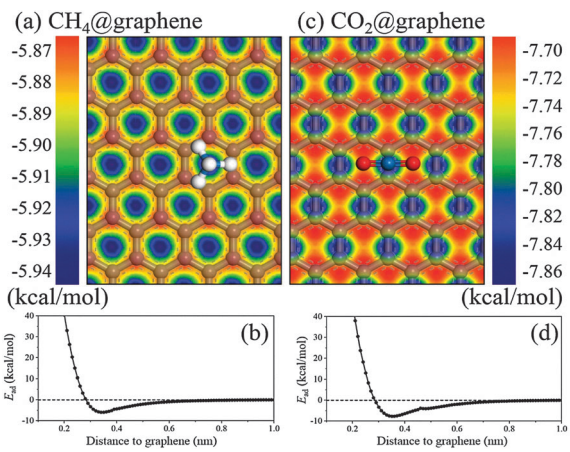

Fig. 1 The potential surface of (a) CH_4 and (c) CO_2 molecules adsorbing on graphene. The blue, white and red balls represent carbon, hydrogen and oxygen atoms, respectively. The gray balls and sticks represent graphene. Adsorption energy (b) between CH_4 and graphene, (d) between CO_2 and graphene with respect to the distance to graphene.

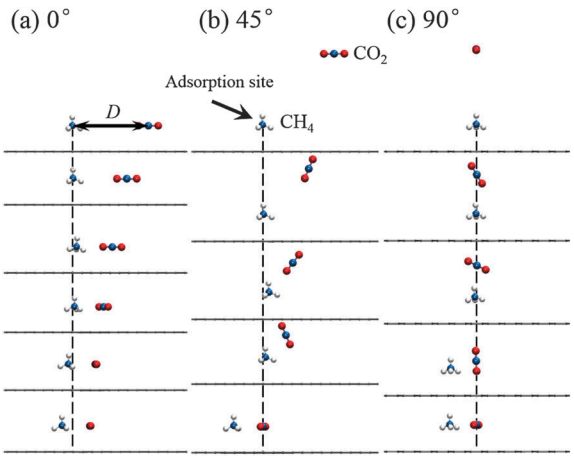

Fig. 3 Side views for the evolutions of displacing a CH_4 molecule by injecting a CO_2 molecule with displacement angles of (a) 0°, (b) 45°, and (c) 90°. The dashed lines represent the position of the adsorption site of CH_4. The blue, white and red balls represent carbon, hydrogen and oxygen atoms, respectively. The gray lines represent graphene.

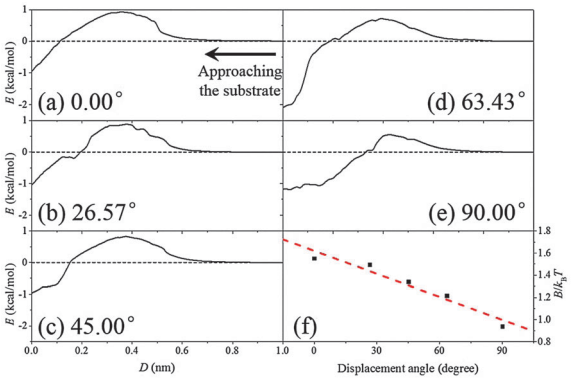

Fig. 4 The variation of the energy with respect to the distance between the CO_2 molecule and the adsorption site of CH_4 when the displacement angle is (a) 0°, (b) 26.57°, (c) 45°, (d) 63.43° and (e) 90°, respectively. (f) The variation of the energy barrier B with respect to the displacement angle θ. k_B and T are the Boltzmann constant and absolute temperature, respectively. Black squares are MD results. The red line is a linear fit to the MD results: $B/k_BT = 1.62057 - 0.00693\theta$.

CO_2 approached CH_4, the energy increased. Then, CO_2 went over an energy barrier to displace CH_4. After that, CO_2 took the adsorption site, while CH_4 was displaced to another adsorption site on graphene. In the displacement process, we found that the CO_2 molecule rotated to achieve the local stable state at a certain position. The energy variation with respect to the distance between the CO_2 and the adsorption site was recorded when CO_2 approached CH_4 in Fig. 4(a)–(e). The energy barrier B decreases with an increase of the displacement angle θ as shown in Fig. 4(f). A linear fit to the MD results showed that $B/k_BT = 1.62057 - 0.00693\theta$, where k_B and $T = 300$ K are the Boltzmann constant and absolute temperature, respectively.

Furthermore, a CO_2 molecule was injected to approach an adsorption layer of CH_4 on graphene, as shown in Fig. 5. The CO_2 molecule approached the adsorption layer in Fig. 5(a)–(c), then was forced by the surrounding CH_4 molecules to rotate vertically to the graphene surface in Fig. 5(d)–(f), and finally resumed in parallel to the graphene surface in Fig. 5(g) and (h). The corresponding energy barrier was about 3.74 kcal mol^{-1}, as shown in Fig. 5(i). Because the adsorption layer was initially saturated with CH_4 molecules, one of the CH_4 in the adsorption CH_4 layer was displaced by CO_2 in this process. Therefore, the energy barrier is much larger than the cases in Fig. 3 because of the surrounding CH_4 molecules.

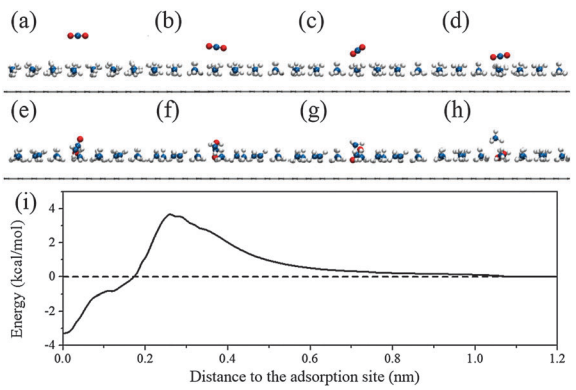

Fig. 5 (a–h) Side view of the displacement of a CH_4 molecule in one adsorption layer by injecting a CO_2 molecule on graphene. The blue, white and red balls represent carbon, hydrogen and oxygen atoms, respectively. The gray lines represent graphene. (i) The energy variation with respect to the distance between the CO_2 molecule and the graphene surface.

Displacement of CH_4 by injecting CO_2 into CNTs

The above discussions are all about adsorption/desorption of CH_4 on open surfaces. However, it has been known that most of the shale gas is stored in the nanopores of the shale. Therefore, to be more realistic, CNTs were chosen as the representation for the nanopores in the shale. The displacement/desorption processes of CH_4 by injecting supercritical CO_2 into CNTs were explored using large-scale MD simulations in this section.

Before exploring the desorption of CH_4 from CNTs, CH_4 molecules were pre-adsorbed on the CNT wall firstly. The adsorption model was established as shown in Fig. 6. The CNT was fixed during the whole process and connected with the bulk phase of CH_4. The adsorption pressure was controlled by the density of the bulk phase. To further explore the displacement of pre-adsorbed CH_4 by CO_2 injection in the CNT, one side of the CNT was connected with the bulk phase of CO_2, while the other side was plugged as shown in Fig. 7(a) and (b). The pressure of the bulk CO_2 was set to be equal to the adsorbed CH_4 in the CNT. In addition, the desorption processes by pressure drawdown were simulated to make a comparison with that by CO_2 injection, shown in Fig. 7(d) and (e).

We mainly focus on how the pore size influences the CO_2 injected desorption of CH_4. Thus, six types of CNTs [(9, 9), (11, 11), (15, 15), (19, 19), (23, 23), (32, 32)] with diameters ranging from 1.2 to 4.3 nm were chosen to mimic the carbon nanopores. The adsorption and desorption processes were modeled at a temperature of 320 K and a pressure of 100 bar.

We began our analysis by exploring the adsorption and desorption in the (15, 15) CNT as an example. At 320 K and 100 bar, the (15, 15) CNT with 4.919 nm long can adsorb 133 CH_4 molecules. However, under the same conditions, the bulk phase can only accommodate 40 CH_4 molecules. This is because the adsorbed phase bears additional pressure exerted

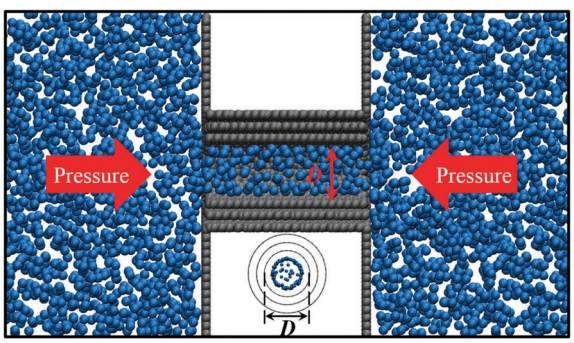

Fig. 6 Adsorption model of MD simulations. The blue and gray balls represent CH_4 molecules and carbon atoms, respectively.

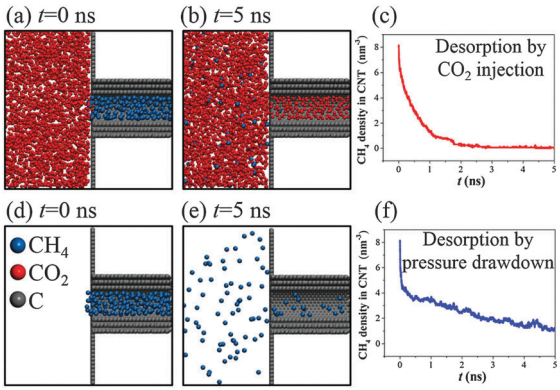

Fig. 7 MD simulations of (a and b) desorption by CO_2 injection, and (d and e) desorption by pressure drawdown. The blue, red and gray balls represent CH_4, CO_2 molecules and C atoms, respectively. Evolutions of the CH_4 density in the CNT with respect to time during the desorption processes (c) by CO_2 injection and (f) by pressure drawdown, respectively.

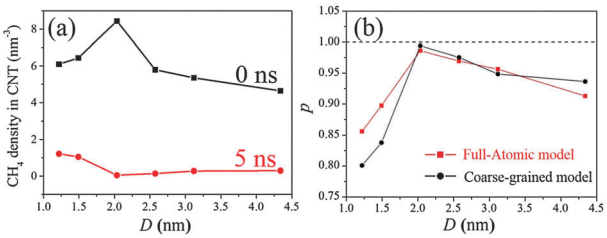

Fig. 8 (a) Variations of the CH_4 density in the CNT with respect to the CNT diameter D at t = 0 ns (black) and t = 5 ns (red), respectively. (b) Variation of p (the percentage of displaced CH_4) with respect to D. Black and red lines represent results using coarse-grained and full-atomic models, respectively.

by the CNT wall compared to the bulk phase. To desorb and exploit the pre-adsorbed CH_4 in the CNT, two methods were used and compared, as shown in Fig. 7. The first method is to inject CO_2 into the CNT, shown in Fig. 7(a) and (b). From the above discussions, we have learnt that the interaction energy between CO_2 and the CNT is stronger than that between CH_4 and the CNT. Thus, those CO_2 molecules that entered into the CNT would displace the adsorbed CH_4 molecules. In this way, the CH_4 molecules were desorbed from the CNT wall and then produced into the left box. At 5 ns, 99.25% CH_4 molecules were released. The second method to desorb CH_4 is by pressure drawdown. Fig. 7(d) and (e) shows the limiting case that the pressure outside the CNT is 0 bar. Due to the existence of the chemical potential gradient, the CH_4 molecules were desorbed from the CNT wall. At 5 ns, 86.46% CH_4 molecules were produced into the left box.

The variation of the CH_4 density in the CNT with respect to time during the desorption processes was plotted in Fig. 7(c) and (f). The gradual decrease of the CH_4 density with time indicates the reduction of the CH_4 molecules in the CNT and the production of the CH_4 molecules into the left box. Moreover, this fig. clearly showed that the CH_4 recovery by CO_2 injection is more efficient than that by pressure drawdown. To be more exact, the injection of CO_2 into the CNT can enhance CH_4 recovery by at least 14.79% over that achieved by pressure drawdown.

Further insight was gained into how the pore size influences adsorption and desorption. The black line in Fig. 8(a) shows the variation of the CH_4 adsorption density as a function of CNT diameter. With the increase of CNT diameter, the adsorption density increases up to a maximum value, and then decreases. This implies the existence of an optimum CNT diameter for maximum methane storage, which is caused by the competition between the curvature effect and the size effect of the CNTs as has been uncovered in previous studies.[24]

The red line in Fig. 8(a) shows the variation of the CH_4 density in the CNT as a function of the CNT diameter after injecting CO_2 at t = 5 ns. With the increase of the CNT diameter, the CH_4 density decreases to a minimum value, and then increases. This indicates the existence of an optimum CNT diameter that minimizes the density of remaining CH_4 in CNTs.

Since the amount of CH_4 recovered is more concerned in the industry, the percentage of CH_4 that was desorbed from the CNT was calculated by

$$p = (\rho_{ad} - \rho_{remain})/\rho_{ad}, \quad (4)$$

in which ρ_{ad} is the adsorption density and ρ_{remain} is the CH_4 density in the CNT after injecting CO_2 at t = 5 ns. The variation of p with respect to the CNT diameter was plotted in Fig. 8(b). This figure shows that there exists an optimum CNT diameter that maximizes p. And the optimum CNT diameter is 2.034 nm. This shows that CH_4 recovery by CO_2 injection is most efficient in the CNT with this optimum diameter.

We also simulated the displacement of CH_4 by CO_2 using a full-atomic model to see whether the displacement would be influenced by the atomic structure which is neglected in the coarse-grained model. As shown in Fig. 8(b), despite some difference between these two models, the tendency does not change, and there remains an optimum CNT diameter of about 2.034 nm that maximizes p. This result implies that the displacement depends on the adsorption energy, density, interactions, but not on the packing structure.

Why does the CH_4 recovery occur most efficiently in the CNT with a certain diameter? To address this question, the variation of the adsorption capacity difference between CO_2 and CH_4 with respect to the CNT diameter should be investigated. If the adsorption capacity difference between CO_2 and CH_4 was higher, CO_2 injected CH_4 recovery should be more efficient. To obtain the adsorption capacity of CO_2 and CH_4, the potential energy surface of the interaction between CH_4 (or CO_2) and the CNT wall was scanned and shown in Fig. 9. The potential energy surface is a curved surface, which can be characterized by two variables. One variable is adsorption energy E_{ad} ($E_{ad} < 0$), the other is the potential well depth H ($H > 0$). With lower the adsorption energy and the higher the well depth, the gas molecule should be bound stronger to the CNT wall, which indicates stronger adsorption capacity of the gas. As shown in Fig. 10, with the increase of the CNT diameter, the difference of the adsorption energy between CO_2 and CH_4, $\Delta E = E_{ad\text{-}CH_4} - E_{ad\text{-}CO_2}$, decreases.

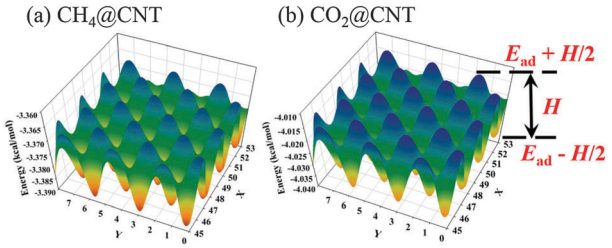

Fig. 9 (a) Potential energy surface of the interaction between a CH_4 molecule and the CNT. (b) The potential energy surface of the interaction between a CO_2 molecule and the CNT.

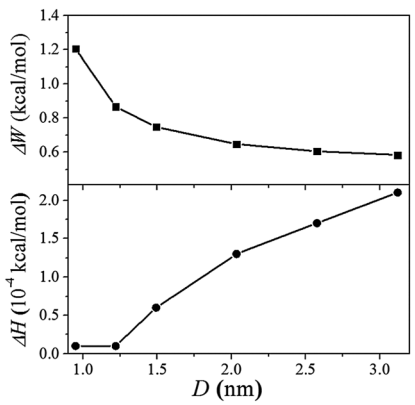

Fig. 10 Variations of (a) $\Delta E = E_{ad\text{-}CH_4} - E_{ad\text{-}CO_2}$ and (b) $\Delta H = H_{CO_2} - H_{CH_4}$ with respect to D, respectively.

However, the difference in the potential well depth between CO_2 and CH_4, $\Delta H = H_{CO_2} - H_{CH_4}$, increases with the CNT diameter. This implies the opposite variation trends of the adsorption capacity difference between CO_2 and CH_4 with respect to D, which explains the existence of the optimum CNT diameter.

Conclusions

Employing MD simulations, the adsorption of CH_4 and CO_2 was compared in the aspects of energy, configuration, structure, capacity and *etc.* And the displacement of CH_4 by CO_2 injection was explored for the first time. $E_{ad\text{-}CO_2}$ on graphene is about 30% lower than $E_{ad\text{-}CH_4}$, which indicates that CO_2 adsorbs more easily on graphene than CH_4 and could be a good candidate in displacing CH_4. First, the displacement of one CH_4 molecule by injecting one CO_2 molecule on graphene was investigated. It was found that the energy barrier required for the displacement process decreases with the increase of the displacement angle. And the displacement of CH_4 occurs most easily when CO_2 approached CH_4 vertically to graphene. Moreover, the energy barrier required for displacing a CH_4 molecule in one adsorption layer by CO_2 injection is larger than that required for displacing an isolated CH_4 adsorbed on graphene. Second, the displacement/desorption of pre-adsorbed CH_4 in CNTs by CO_2 injection was explored. Comparison between the desorption process by CO_2 injection and that by pressure drawdown indicates that the injection of CO_2 into the CNT can enhance CH_4 recovery by at least 14.78% over that achieved by pressure drawdown. In addition, the CO_2-injected displacement of CH_4 depends on the CNT diameter. There exists an optimum diameter that makes CO_2-injected CH_4 recovery occur most efficiently. The underlying mechanisms of this phenomenon were uncovered.

Acknowledgements

This work was jointly supported by the National Natural Science Foundation of China (NSFC, Grant U1562105, 11202213 and 11372313) and the Key Research Program of the Chinese Academy of Sciences (Grant KJZD-EW-M01).

Notes and references

1 J. B. Curtis, *AAPG Bull.*, 2002, **86**, 1921–1938.
2 A. Burnham, J. Han, C. E. Clark, M. Wang, J. B. Dunn and I. Palou-Rivera, *Environ. Sci. Technol.*, 2012, **46**, 619–627.
3 K. Mosher, J. J. He, Y. Y. Liu, E. Rupp and J. Wilcox, *Int. J. Coal Geol.*, 2013, **109**, 36–44.
4 U. Kuila and M. Prasad, *Geophys. Prospect.*, 2013, **61**, 341–362.
5 R. G. Loucks, R. M. Reed, S. C. Ruppel and D. M. Jarvie, *J. Sediment. Res.*, 2009, **79**, 848–861.
6 P. Chareonsuppanimit, S. A. Mohammad, R. L. Robinson and K. A. M. Gasem, *Int. J. Coal Geol.*, 2012, **95**, 34–46.
7 R. Heller, J. Vermylen and M. Zoback, *AAPG Bull.*, 2014, **98**, 975–995.
8 A. A. Hinai, R. Rezaee, L. Esteban and M. Labani, *J. Unconv. Oil Gas Resour.*, 2014, **8**, 1–13.
9 F. Javadpour, *J. Can. Pet. Technol.*, 2009, **48**, 16–21.
10 F. Javadpour, D. Fisher and M. Unsworth, *J. Can. Pet. Technol.*, 2007, **46**, 55–61.
11 A. Rogala, K. Ksiezniak, J. Krzysiek and J. Hupka, *Physicochem. Probl. Miner. Process.*, 2014, **50**, 681–692.
12 T. Ishida, K. Aoyagi, T. Niwa, Y. Q. Chen, S. Murata, Q. Chen and Y. Nakayama, *Geophys. Res. Lett.*, 2012, **39**, 6.
13 S. M. Kang, E. Fathi, R. J. Ambrose, I. Y. Akkutlu and R. F. Sigal, *SPE J.*, 2011, **16**, 842–855.
14 R. Heller and M. Zoback, *J. Unconv. Oil Gas Resour.*, 2014, **8**, 14–24.
15 C. Hussen, R. Amin, G. Madden and B. Evans, *J. Nat. Gas Sci. Eng.*, 2012, **5**, 42–50.
16 P. Kowalczyk, P. A. Gauden, A. P. Terzyk, S. Furmaniak and P. J. F. Harris, *J. Phys. Chem. C*, 2012, **116**, 13640–13649.
17 R. D. Vidic, S. L. Brantley, J. M. Vandenbossche, D. Yoxtheimer and J. D. Abad, *Science*, 2013, **340**, 1235009.
18 M. Godec, G. Koperna, R. Petrusak and A. Oudinot, *Energy Procedia*, 2013, **37**, 6644–6655.
19 X. Li and D. Elsworth, *J. Nat. Gas Sci. Eng.*, 2015, **26**, 1607–1619.
20 R. F. Cracknell, P. Gordon and K. E. Gubbins, *J. Phys. Chem.*, 1993, **97**, 494–499.
21 Z. Tan and K. E. Gubbins, *J. Phys. Chem.*, 1990, **94**, 6061–6069.

22 E. A. Müller, F. R. Hung and K. E. Gubbins, *Langmuir*, 2000, **16**, 5418–5424.
23 A. Busch, Y. Gensterblum and B. M. Krooss, *Int. J. Coal Geol.*, 2003, **55**, 205–224.
24 X. Y. Zhu and Y. P. Zhao, *J. Phys. Chem. C*, 2014, **118**, 17737–17744.
25 K. Jessen, G. Q. Tang and A. R. Kovscek, *Transp. Porous Media*, 2008, **73**, 141–159.
26 J. Q. Shi and S. Durucan, *Fuel*, 2003, **82**, 1219–1229.
27 S. Plimpton, *J. Comput. Phys.*, 1995, **117**, 1–19.
28 P. Dauber-Osguthorpe, V. A. Roberts, D. J. Osguthorpe, J. Wolff, M. Genest and A. T. Hagler, *Proteins*, 1988, **4**, 31–47.
29 Y. Kurniawan, S. K. Bhatia and V. Rudolph, *AIChE J.*, 2006, **52**, 957–967.
30 W. A. Steele, *Surf. Sci.*, 1973, **36**, 317–352.